Progress In Electromagnetics Research C, Vol. 148, 189-203, 2024

PIER C

(Received 6 July 2024, Accepted 11 October 2024, Scheduled 17 October 2024)

Robust Deadbeat Fault-Tolerant Predictive Current Control for IPMSM Considering Demagnetization Fault Based on Cascade Flux Linkage Observer

Dingdou Wen[1], Xiaorui Wei[1], Xincheng Zhu[1],
Chuandong Shi[1], Wenting Zhang[1], and Zhun Cheng[2, *]

[1]*Hunan University of Technology, Zhuzhou 412007, China*
[2]*Hunan Railway Professional Technology College, Zhuzhou 412001, China*

ABSTRACT: To address the issues of decreased electromagnetic torque, poor robustness, and failure of demagnetization fault detection caused by permanent magnet demagnetization and inductance mismatch in interior permanent magnet synchronous motor (IPMSM), a robust deadbeat fault-tolerant predictive current control (RDFTPCC) strategy based on cascade flux linkage observer (CFO) is proposed. The proposed CFO is constructed by combining a discrete model reference adaptive system (MRAS) with an improved non-singular fast terminal sliding mode observer (INFTSMO). MRAS and INFTSMO perform d-q axis inductance estimation and demagnetization fault detection, respectively. A better current prediction can be obtained via the parameter state information from CFO. Moreover, the RDFTPCC is constructed by the state information obtained from CFO, which can compensate for the torque deficit due to permanent magnet demagnetization and the control performance degradation due to parameter mismatch, hence realizing fault-tolerant control. The experimental results indicate that the proposed method exhibits stronger fault-tolerance and robustness than the conventional method when the IPMSM suffers from demagnetization fault and inductance mismatch.

1. INTRODUCTION

Recently, interior permanent magnet synchronous motor (IPMSM) has been extensively utilized in the fields of railway transportation and aerospace due to its benefits such as strong power density and overload capacity [1, 2]. The output effect of the electromagnetic torque is closely influenced by the dynamic characteristics of the current control loop of the IPMSM. The performance of the control system can be significantly enhanced with favorable current control [3].

To realize fast and accurate control of motors, many advanced control methods such as robust control [4], fuzzy proportional integral (PI) control [5], and deadbeat predictive current control (DPCC) [6] are proposed. In contrast, DPCC method is widely studied due to its ability to rapidly and precisely track a given current and good stability [7, 8].

On the other hand, IPMSM generally operates in complex and variable environments such as corrosion and electromagnetism, and its own temperature is highly susceptible to increase. The control performance of the IPMSM may be impacted by uncertainties such as demagnetization fault and parameter mismatch [9, 10]. For example, demagnetization of permanent magnet (PM) can cause a significant decrease in the output torque of the motor [11]. DPCC depends on an exact IPMSM model, and once the model parameters are mismatched, the calculated voltage vectors are in error, which degrades the control performance of the DPCC [12].

Refs. [13–16] extract the stator current signal of PMSM by using signal processing methods such as Hilbert Huang, wavelet transform, Fourier transform, convolutional neural network, and machine learning, respectively, for demagnetization fault detection. However, they rely on the computational power of the controller. To address the above issues, detection methods such as extended Kalman filter (EKF) [17, 18], model reference adaptive algorithm [19], and sliding mode observer (SMO) [20, 21] are proposed.

The above methods are effective in detecting motor demagnetization fault, but they do not provide fault tolerant control for faulty motor. In [22], an EKF observer is utilized for the estimation of PM flux linkage, which is input in real time into a dual-vector model predictive controller to diminish the effect of PM demagnetization on the motor control system. In [23], demagnetization fault reconstruction is carried out by using an SMO and inputs the observed flux linkage into a fault-tolerant controller, which continuously updates the flux linkage parameters in the controller, achieving the purpose of fault-tolerant control. In [24], a novel hyperlocal model is constructed, and an SMO is utilized to observe the uncertain part of the hyperlocal model, which allows the robustness of the system to be improved.

Nevertheless, [22–24] solve the parameter mismatch problem caused by the demagnetisation of permanent magnets, thus improving the current tracking accuracy. In [22–24], the problem of parameter mismatch caused by PM demagnetization is solved, which improves the tracking accuracy of current, but

---

* Corresponding author: Zhun Cheng (120277982@qq.com).

doi:10.2528/PIERC24070602

it cannot solve the problem of torque loss due to PM demagnetization. Especially when the motor drives a large load in a demagnetized state, the motor still cannot operate normally without compensating for the missing torque. In [25], an SMO is utilized to estimate the active flux linkage of the motor, and a deadbeat control strategy is used to achieve fault-tolerant control. However, the method only investigates the amplitude reduction of the PM flux linkage during demagnetization fault, without considering the variation of magnetic deviation angle. In [26], the back electromotive force caused by PM demagnetization is stored in a table, and a fault-tolerant deadbeat controller is designed using the lookup table method, which eliminates the impact of demagnetization fault in axial flux PMSM, but the method does not combine accuracy and speed at the same time.

In summary, a robust deadbeat fault-tolerant predictive current control (RDFTPCC) method based on a cascade flux linkage observer (CFO) is proposed. Unlike existing methods, the method can accurately observe the faulty flux linkage even when the inductances are mismatched and compensate for the torque deficit due to the PM demagnetization. Therefore, it has stronger parameter robustness. The main contributions of this study are concluded as follows:

1. An incremental current prediction error model with inductance decoupling and no flux linkage parameter is derived, and a discrete model reference adaptive system (MRAS) is designed based on it to identify the actual d-q axis inductance. Combined with the designed improved nonsingular fast terminal sliding mode observer (INFTSMO), a CFO is constructed, which is able to accurately detect demagnetization fault during inductance mismatch, with stronger robustness.
2. RDFTPCC method is designed through the state information obtained from CFO, which can timely output the correct d-axis reference current in the case of PM demagnetization and inductance mismatch. Thus, the missing torque is compensated, and the q-axis current can be quickly restored to the normal value, which improves the fault tolerance of the system.
3. The CFO is designed to accurately observe the current predicted value at the next moment and replace the sampled current in the RDFTPCC, overcoming the effect of one-step delay. The predicted current values observed during PM demagnetization and inductance mismatch are more stable.

The remainder of this article is structured as follows. In Section 2, the IPMSM normal and fault mathematical model is established. In Section 3, the principle of conventional DPCC is introduced. In Section 4, the design principle of cascaded flux linkage observer is elaborated. In Section 5, the implementation process of robust deadbeat fault-tolerant predictive current control strategy is explored. In Section 6, the experimental results and analysis are given. Finally, the conclusion section is presented.

2. MATHEMATICAL MODELS OF CONVENTIONAL AND DEMAGNETIZED IPMSM

2.1. The Mathematical Model of Healthy IPMSM

The stator voltage equation of IPMSM is represented as [27]

$$\left\{\begin{array}{l} u_d = R_s i_d + \frac{d\psi_d}{dt} - \omega_e \psi_q \\ u_q = R_s i_q + \frac{d\psi_q}{dt} + \omega_e \psi_d \end{array}\right. \tag{1}$$

where the stator flux equation is

$$\left\{\begin{array}{l} \psi_d = \psi_{ro} + L_d i_d \\ \psi_q = L_q i_q \end{array}\right. \tag{2}$$

where ψ_d and ψ_q are the d-q axis stator flux. ψ_{ro} is the PM flux linkage. u_d, u_q, i_d, and i_q are the d-q axis stator voltages and stator currents, respectively. R_s, ω_e, L_d, and L_q, are stator resistance, electrical angular velocity, and d-q axis stator inductances, respectively.

The electromagnetic torque equation is

$$T_e = \frac{3}{2} n_p [\psi_{ro} + (L_d - L_q) i_d] i_q \tag{3}$$

where T_e is the electromagnetic torque, and n_p is the number of pole pairs.

From (3), the effective flux linkage of the IPMSM is as [28]:

$$\psi_{ext} = \psi_{ro} + (L_d - L_q) i_d \tag{4}$$

2.2. The Mathematical Model of Demagnetized IPMSM

When the IPMSM is demagnetized, the amplitude of the PM flux linkage will change from ψ_{ro} to ψ_r; the magnetic deviation angle will change from 0° to γ, and $\gamma \in [0^{\circ}, 90^{\circ})$ [29] (see Fig. 1). Therefore, (2) is rewritten as

$$\left\{\begin{array}{l} \psi_d = L_d i_d + \psi_{ro} + \Delta\psi_{rd} = L_d i_d + \psi_{rd} \\ \psi_q = L_q i_q + \Delta\psi_{rq} = L_q i_q + \psi_{rq} \end{array}\right. \tag{5}$$

$$\left\{\begin{array}{l} \psi_{rd} = \psi_{ro} + \Delta\psi_{rd} = \psi_r \cos\gamma \\ \psi_{rq} = \Delta\psi_{rq} = \psi_r \sin\gamma \end{array}\right. \tag{6}$$

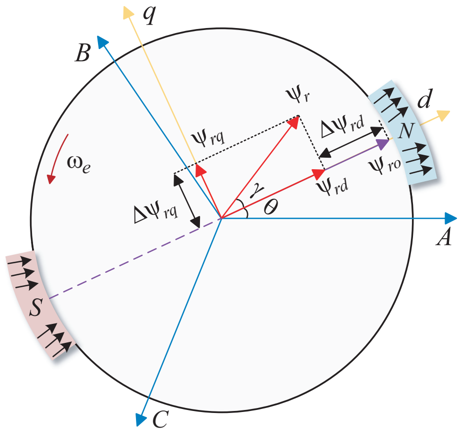

FIGURE 1. Variation relationship of PM flux linkage.

From (1), (5), and (6), the stator voltage equation for IPMSM demagnetization is

$$\begin{cases} u_d = R_s i_d + L_d \frac{di_d}{dt} - \omega_e (L_q i_q + \psi_{rq}) \\ u_q = R_s i_q + L_q \frac{di_q}{dt} + \omega_e (L_d i_d + \psi_{rd}) \end{cases} \tag{7}$$

The electromagnetic torque equation for IPMSM demagnetization is represented as follows

$$T_e = \frac{3}{2} n_p [\psi_{rd} i_q + (L_d - L_q) i_d i_q - \psi_{rq} i_d] \tag{8}$$

3. PRINCIPLE OF CONVENTIONAL DPCC

The forward Euler method is adopted to discretize (1), and the discrete current model of IPMSM is represented as

$$\begin{cases} i_d(k+1) = \left(1 - \frac{R_s T_s}{L_d}\right) i_d(k) \\ + \frac{T_s \omega_e(k) L_q}{L_d} i_q(k) + \frac{T_s}{L_d} u_d(k) \\ i_q(k+1) = \left(1 - \frac{R_s T_s}{L_q}\right) i_q(k) \\ - \frac{T_s \omega_e(k) L_d}{L_q} i_d(k) + \frac{T_s}{L_q} u_q(k) - \frac{T_s \omega_e(k)}{L_q} \psi_{ro} \end{cases} \tag{9}$$

where T_s is the sampling period, and k and $k+1$ represent the current value and next moment value, respectively.

From (9), the expected voltage of the DPCC method can be written as

$$\begin{cases} u_d^*(k) = L_d \frac{i_d^*(k+1) - i_d(k)}{T_s} \\ -\omega_e(k) L_q i_q(k) + R_s i_d(k) \\ u_q^*(k) = L_q \frac{i_q^*(k+1) - i_q(k)}{T_s} \\ +\omega_e(k) L_d i_d(k) + R_s i_q(k) + \omega_e(k) \psi_{ro} \end{cases} \tag{10}$$

where i_d^* and i_q^* are the d-q axis current reference values. u_d^* and u_q^* are the d-q axis voltage reference values output by DPCC.

As shown in (10), the PM flux linkage, stator inductance, and resistance are included in the model of the conventional DPCC, indicating that the DPCC is sensitive to the motor model parameters. Refs. [30, 31] point out that the mismatch of resistance parameters has a negligible effect on conventional DPCC. Therefore, in this paper, only the effects of PM demagnetization and inductance mismatch on the performance of DPCC are considered.

4. DESIGN OF CFO

4.1. Discrete MRAS-Based Identification of *D-Q* Axis Stator Inductances

Because the electrical time constant of the IPMSM is much less than its mechanical time constant, ω_e can be assumed to be fixed during adjacent control cycles. The predicted current increment can be represented as [32]

$$\begin{cases} \Delta i_d(k+1) = \left(1 - \frac{R_s T_s}{L_d}\right) \Delta i_d(k) \\ + \frac{T_s \omega_e(k) L_q}{L_d} \Delta i_q(k) + \frac{T_s}{L_d} \Delta u_d(k) \\ \Delta i_q(k+1) = \left(1 - \frac{R_s T_s}{L_q}\right) \Delta i_q(k) \\ - \frac{T_s \omega_e(k) L_d}{L_q} \Delta i_d(k) + \frac{T_s}{L_q} \Delta u_q(k) \end{cases} \tag{11}$$

where Δu_d and Δu_q are the d-q axis voltage increments, and Δi_d and Δi_q are the d-q axis current increments, respectively.

When IPMSM experiences inductance mismatch and PM demagnetization, the actual predicted current increment is

$$\begin{cases} \Delta i_d^{act}(k+1) = \left(1 - \frac{R_s T_s}{L_d^{act}}\right) \Delta i_d(k) \\ + \frac{T_s \omega_e(k) L_q^{act}}{L_d^{act}} \Delta i_q(k) + \frac{T_s}{L_d^{act}} \Delta u_d(k) \\ \Delta i_q^{act}(k+1) = \left(1 - \frac{R_s T_s}{L_q^{act}}\right) \Delta i_q(k) \\ - \frac{T_s \omega_e(k) L_d^{act}}{L_q^{act}} \Delta i_d(k) + \frac{T_s}{L_q^{act}} \Delta u_q(k) \end{cases} \tag{12}$$

where L_d^{act} and L_q^{act} are the actual d-q axis stator inductances, and $L_d^{act} = L_d + \Delta L_d$, $L_q^{act} = L_q + \Delta L_q$. Δi_d^{act} and Δi_q^{act} are the actual d-q axis current increments, respectively.

Subtracting (11) from (12), the incremental current prediction errors is

$$\begin{cases} \Delta \tilde{i}_d(k+1) = T_s \left(\frac{R_s}{L_d} - \frac{R_s}{L_d^{act}}\right) \Delta i_d(k) \\ + \omega_e(k) T_s \left(\frac{L_q^{act}}{L_d^{act}} - \frac{L_q}{L_d}\right) \Delta i_q(k) \\ + T_s \left(\frac{1}{L_d^{act}} - \frac{1}{L_d}\right) \Delta u_d(k) \\ \Delta \tilde{i}_q(k+1) = T_s \left(\frac{R_s}{L_q} - \frac{R_s}{L_q^{act}}\right) \Delta i_q(k) \\ - \omega_e(k) T_s \left(\frac{L_d^{act}}{L_q^{act}} - \frac{L_d}{L_q}\right) \Delta i_q(k) \\ + T_s \left(\frac{1}{L_q^{act}} - \frac{1}{L_q}\right) \Delta u_q(k) \end{cases} \tag{13}$$

where $\Delta \tilde{i}_d$ and $\Delta \tilde{i}_q$ are the d-q axis incremental current prediction errors.

Because the current amplitude is much less than the voltage amplitude, and the voltage varies quickly, the amplitude of its fluctuations is much more than the amplitude of the current fluctuations [33], then (13) can be abbreviated as

$$\begin{cases} \Delta \tilde{i}_d(k+1) = T_s \left(\frac{1}{L_d^{act}} - \frac{1}{L_d}\right) \Delta u_d(k) \\ \Delta \tilde{i}_q(k+1) = T_s \left(\frac{1}{L_q^{act}} - \frac{1}{L_q}\right) \Delta u_q(k) \end{cases} \tag{14}$$

Rewrite $\Delta \tilde{i}_d(k+1)$ and $\Delta \tilde{i}_q(k+1)$ as

$$\begin{cases} \Delta \tilde{i}_d(k+1) = [i_d^{act}(k+1) - i_d(k+1)] \\ - [i_d^{act}(k) - i_d(k)] = \delta i_d(k+1) - \delta i_d(k) \\ \Delta \tilde{i}_q(k+1) = \left[i_q^{act}(k+1) - i_q(k+1)\right] \\ - \left[i_q^{act}(k) - i_q(k)\right] = \delta i_q(k+1) - \delta i_q(k) \end{cases} \tag{15}$$

where δi_d and δi_q are the d-q axis current prediction errors.

From (14) and (15), the d-q axis current prediction errors at moment k can be further introduced as

$$\begin{cases} \delta i_d(k) = \delta i_d(k-1) + \lambda_d T_s \left[u_d(k-1) - u_d(k-2)\right] \\ \delta i_q(k) = \delta i_q(k-1) + \lambda_q T_s \left[u_q(k-1) - u_q(k-2)\right] \end{cases} \tag{16}$$

where $u_d(k-2)$ and $u_q(k-2)$ are the d-q axis stator voltages at moment $k-2$. λ_d and λ_q are the d-q axis inductance coefficients, and $\lambda_d = (1/L_d^{act} - 1/L_d)$, $\lambda_q = (1/L_q^{act} - 1/L_q)$.

For univariate discrete systems, the following reference model is adopted [34]

$$y^*(t) = \alpha_1 y^*(t-i) + \sum_{i=0}^{2} \beta_i u(t-i) \tag{17}$$

where $u(t)$ and $y^*(t)$ are the input and output of the reference model. α_1, β_i are the reference model coefficients, which are fixed values.

Replacing the fixed coefficient in (17) with the adjustable coefficient, the parallel adjustable model is

$$\begin{cases} y_0(t) = \hat{\alpha}_1(t-1)y(t-1) + \sum\limits_{i=0}^{2} \hat{\beta}_i(t-1)u(t-i) \\ y(t) = \hat{\alpha}_1(t)y(t-1) + \sum\limits_{i=0}^{2} \hat{\beta}_i(t)u(t-i) \end{cases} \tag{18}$$

From (18), the parallel adjustable model consists of two parts, where the first part is the prior output $y_0(t)$, i.e., the output obtained from the adjustable coefficients at the previous moment. The second part is the posteriori output $y(t)$, i.e., the output obtained from the adjustable coefficients at the current time. $\hat{\alpha}_1(t)$ and $\hat{\beta}_i(t)$ are the adjustable coefficients to be identified for item t.

From (17) and (18), the following expression is obtained

$$\begin{cases} e(t) = y^*(t) - y(t),\ e_0(t) = y^*(t) - y_0(t) \\ v(t) = e(t) + \sum\limits_{i=1}^{r} p_i e(t-i),\ v_0(t) = e_0(t) + \sum\limits_{i=1}^{r} p_i e(t-i) \end{cases} \tag{19}$$

where $e_0(t)$ and $e(t)$ are the prior output error and posterior output error, respectively. $v_0(t)$ and $v(t)$ are the linear compensator outputs of the prior output error and posterior output error, respectively. r and p_i are the parameters to be designed, which only need to satisfy the stability conditions. To simplify the subsequent proof process, this paper selects the case of $r = 0$ and $p_i = 0$.

The estimation value of traditional adaptive algorithms contains only integral terms $\hat{\alpha}_1(t)$ and $\hat{\beta}_i(t)$. To further accelerate the convergence speed of the identified value, the proportion terms $\hat{\alpha}_{p1}(t)$ and $\hat{\beta}_{pi}(t)$ of the memoryless part are introduced. The designed adaptive law for designing adjustable coefficients is as follows

$$\begin{cases} \hat{\alpha}_1(t) = \hat{\alpha}_1(t-1) + v(t)y(t-1) + \hat{\alpha}_{p1}(t) \\ = \hat{\alpha}_1(-1) + \sum\limits_{x=0}^{t} (1+\theta)\left[v(x)y(x-1)\right] \\ \hat{\alpha}_{p1}(t) = \theta v(t)y(t-1) \\ \hat{\beta}_i(t) = \hat{\beta}_i(t-1) + v(t)u(t-i) + \hat{\beta}_{pi}(t) \\ = \hat{\beta}_i(-1) + \sum\limits_{x=0}^{t} (1+\theta)\left[v(x)u(x-i)\right] \\ \hat{\beta}_{pi}(t) = \theta v(t)u(t-i) \end{cases} \tag{20}$$

where θ is the proportional gain coefficient, $i = 0, 1, 2$.

Substituting $p_i = 0$ into (19), the discrete MRAS reference and adjustable models are shown in (21), and the adaptive law is shown in (22).

$$\begin{cases} y^*(t) = \alpha_1 y^*(t-1) + \sum\limits_{i=0}^{2} \beta_i u(t-i) \\ y(t) = \hat{\alpha}_1(t)y(t-1) + \sum\limits_{i=0}^{2} \hat{\beta}_i(t)u(t-i) \end{cases} \tag{21}$$

$$\begin{cases} \nu_0(t) = y^*(t) - \hat{\alpha}_1(t-1)y(t-1) - \sum\limits_{i=0}^{2} \hat{\beta}_i(t-1)u(t-i) \\ \hat{\alpha}_1(t) = \hat{\alpha}_1(t-1) + \dfrac{(1+\theta)\nu_0(t)u(t-i)}{1+(1+\theta)[y(t-1)^2 + \sum\limits_{i=0}^{2} u(t-i)^2]} \\ \hat{\beta}_i(t) = \hat{\beta}_i(t-1) + \dfrac{(1+\theta)\nu_0(t)u(t-i)}{1+(1+\theta)[y(t-1)^2 + \sum\limits_{i=0}^{2} u(t-i)^2]} \end{cases} \tag{22}$$

The proof of system stability is as follows:

1) Verification of the forward loop satisfies strict positive realness

   From (19), the following expression is obtained

$$\begin{cases} e(t) = \alpha_1 e(t-1) - \zeta(t) \\ \zeta(t) = \left[\sum\limits_{x=0}^{t} (1+\theta)[v(x)y(x-1)] + \hat{\alpha}_1(-1) - \alpha_1\right] y(t-1) \\ + \sum\limits_{i=0}^{2} \left[\sum\limits_{x=0}^{t} (1+\theta)[v(x)u(x-i)] + \hat{\beta}_i(-1) - \beta_i\right] u(t-i) \end{cases} \tag{23}$$

   When $p_i = 0$, the transfer function of the forward loop is:

$$G(z) = \frac{v(z)}{-\zeta(z)} = \frac{1}{1 - \alpha_1 z^{-1}} = \frac{z}{z - \alpha_1} \tag{24}$$

   Since $\alpha_1 = 1$ is a fixed value in the reference model, when the system is boundary stable, and the amplitude frequency characteristics are positive over the entire frequency range, the forward loop transfer function satisfies strict positive definite condition.

2) Verification of the feedback loop satisfies the Popov inequality

   Popov inequality is established as follows

$$\eta(0, t_1) = \sum_{t=0}^{t_1} \zeta(t)v(t) \ge -r_0^2, \quad \forall t_1 \ge 0 \tag{25}$$

   Substituting (23) into (25), the following expression is obtained

$$\begin{aligned} \eta(0, t_1) = \sum_{t=0}^{t_1} v(t)y(t-1) & \left[\sum_{x=0}^{t} (1+\theta)[v(x)y(x-1)] + \hat{\alpha}_1(-1) - \alpha_1\right] \\ & + \sum_{i=0}^{2} \left\{\sum_{t=0}^{t_1} v(t)u(t-i) \left[\sum_{x=0}^{t} (1+\theta) \right.\right. \\ & \left.\left. [v(x)u(x-i)] + \hat{\beta}_i(-1) - \beta_i\right]\right\} \ge -r_0^2 \end{aligned} \tag{26}$$

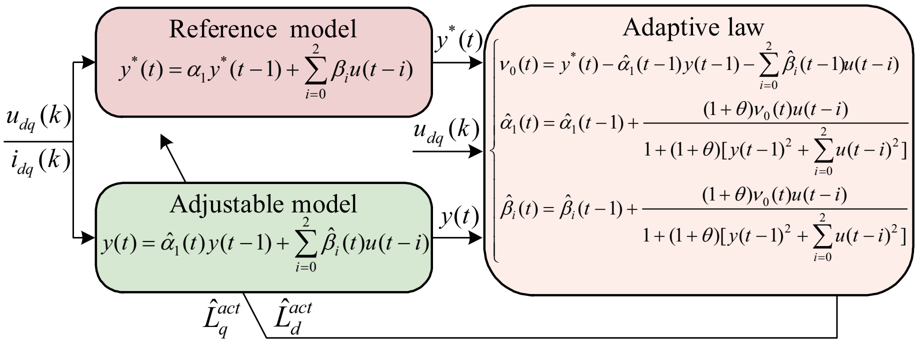

FIGURE 2. The block diagram of discrete MRAS-based d-q axis stator inductances identification.

Lemma 1: (27) inequality holds for any $x+1$ real number w_i [35]:

$$\sum_{i=1}^{x} w_i\left(\sum_{t=1}^{i} w_t + w_0\right)=\frac{1}{2}\left(\sum_{i=1}^{x} w_i + w_0\right)^2$$

$$+\frac{1}{2}\sum_{i=1}^{x} w_i^2-\frac{w_0^2}{2}\geq-\frac{w_0^2}{2} \quad (27)$$

When $|\theta| \ll 1$ ($\theta = 0.0001$ in this paper), the following expression can be obtained from (26) and (27)

$$\eta(0,t_1)\geq-\frac{1}{2}\left[(\hat{\alpha}_1(-1)-\alpha_1)^2\right.$$

$$\left.+\sum_{i=0}^{2}\left(\hat{\beta}_i(-1)-\beta_i\right)^2\right]=-r_0^2 \quad (28)$$

Therefore, MRAS is asymptotically stable when $|\theta| \ll 1$.

Applying the adaptive law (22) to (21), the adjustable model $y(t)$ will converge to $y^*(t)$, and the identifiable adjustable coefficients $\hat{\alpha}_1(t)$ and $\hat{\beta}_i(t)$ will converge to α_1 and β_i. The final identification expression for the inductance is

$$\begin{cases} \hat{L}_s^{act}=T_s L_s/\left[T_s+L_s\hat{\beta}_1(t)\right] \\ s=d \quad or \quad q \end{cases} \quad (29)$$

The block diagram of discrete MRAS-based d-q axis stator inductances identification is shown in Fig. 2.

4.2. Design and Stability Analysis of INFTSMO Based on Improved Double Power Reaching Law

The key to implement the RDFTPCC method is the observation accuracy and speed of the CFO. To make the CFO observe each state information faster and more accurately, in this section, the improved double power reaching law is introduced and combined with the NFTSM to form the INFTSMO, which has a faster convergence speed and higher observation accuracy.

Equation (7) is rewritten as the state equation as

$$\begin{cases} \dot{\mathbf{x}}=\mathbf{Ax}+\mathbf{Bu}+\mathbf{Cd} \\ \mathbf{y}=\mathbf{Dx} \end{cases} \quad (30)$$

where $\mathbf{x}=[\ i_d \quad i_q\ ]^{\mathrm{T}}$, $\mathbf{u}=[\ u_d \quad u_q\ ]^{\mathrm{T}}$, $\mathbf{y}=[\ i_d \quad i_q\ ]^{\mathrm{T}}$ and $\mathbf{d}=[\ \psi_{rd} \quad \psi_{rq}\ ]^{\mathrm{T}}$. $\boldsymbol{A}$, $\boldsymbol{B}$, $\boldsymbol{C}$ and $\boldsymbol{D}$ are the coefficient matrices.

$$\mathbf{A}=\begin{bmatrix} -\frac{R_s}{\hat{L}_d^{act}} & \omega_e\frac{\hat{L}_q^{act}}{\hat{L}_d^{act}} \\ -\omega_e\frac{\hat{L}_d^{act}}{\hat{L}_q^{act}} & -\frac{R_s}{\hat{L}_q^{act}} \end{bmatrix}, \quad \mathbf{B}=\begin{bmatrix} \frac{1}{\hat{L}_d^{act}} & 0 \\ 0 & \frac{1}{\hat{L}_q^{act}} \end{bmatrix},$$

$$\mathbf{C}=\begin{bmatrix} 0 & \frac{\omega_e}{\hat{L}_d^{act}} \\ -\frac{\omega_e}{\hat{L}_q^{act}} & 0 \end{bmatrix}, \quad \mathbf{D}=\begin{bmatrix} 1 & 0 \\ 0 & 1 \end{bmatrix}.$$

The INFTSMO designed based on (30) can be expressed as

$$\dot{\hat{\mathbf{x}}}=\mathbf{A}\hat{\mathbf{x}}+\mathbf{Bu}+\mathbf{v} \quad (31)$$

where $\hat{\mathbf{x}}$ is the observed value of $\boldsymbol{x}$, $\hat{\mathbf{x}}=[\ \hat{i}_d \quad \hat{i}_q\ ]^{\mathrm{T}}$. $\mathbf{v}=[\ v_d \quad v_q\ ]^{\mathrm{T}}$ is the sliding mode term.

Subtracting (30) from (31), the current error state equation is as

$$\dot{\mathbf{e}}=\mathbf{Ae}+\mathbf{Cd}-\mathbf{v} \quad (32)$$

where e is the current observation error, $\mathbf{e}=x-\hat{x}$.

To ensure the rapid convergence of current errors, the non-singular fast terminal sliding mode surface is designed as follows

$$\mathbf{s}=\mathbf{ae}+\mathbf{b}\dot{\mathbf{e}}+\mathbf{c}\dot{\mathbf{e}}^{p/q} \quad (33)$$

where $\mathbf{a}$, $\mathbf{b}$, and $\mathbf{c}$ are the positive parameter matrices to be designed, $\mathbf{a}=\mathrm{diag}(\ a_d \quad a_q\ )$, $\mathbf{b}=\mathrm{diag}(\ b_d \quad b_q\ )$, $\mathbf{c}=\mathrm{diag}(\ c_d \quad c_q\ )$. $\mathbf{s}$ is sliding mode surface, and $\mathbf{s}=[\ s_d \quad s_q\ ]^{\mathrm{T}}$. p and q are the odd constants to be designed, $1<p/q<2$.

Deriving (33), the following expression is obtained

$$\dot{\mathbf{s}}=\mathbf{a}\dot{\mathbf{e}}+\mathbf{b}\ddot{\mathbf{e}}+p/q\cdot\mathbf{c}\dot{\mathbf{e}}^{p/q-1}\ddot{\mathbf{e}} \quad (34)$$

To ensure that the system state variables enter the sliding mode surface quickly and suppress chattering, an improved double power reaching law [36] is selected as shown in (35). Compared to the existing improved sliding mode convergence law, the introduced improved double power reaching law is able to reach the sliding mode surface quickly while reducing the steady state error and weakening the jitter

$$\begin{cases} \dot{\mathbf{s}}=-\mathbf{k}_1(|\mathbf{x}|\,|\mathbf{s}|)^{1-d}\mathrm{sgn}(\mathbf{s})-\mathbf{k}_2\,|\mathbf{s}|^{1+d}\,\mathrm{sgn}(\mathbf{s}) \\ \lim\limits_{t\to\infty}\mathbf{x}=[\ 0 \quad 0\ ]^{\mathrm{T}} \end{cases} \quad (35)$$

where $\mathbf{k}_1$ and $\mathbf{k}_2$ are the positive parameter matrices to be designed, $\mathbf{k}_1 = \mathrm{diag}\begin{pmatrix} k_{1d} & k_{1q} \end{pmatrix}$, $\mathbf{k}_2 = \mathrm{diag}\begin{pmatrix} k_{2d} & k_{2q} \end{pmatrix}$, and sgn( ) is the symbol function. $\boldsymbol{x}$ is the system state variable, $\mathbf{x} = \begin{bmatrix} x_d & x_q \end{bmatrix}^{\mathrm{T}} = \begin{bmatrix} i_d & i_q \end{bmatrix}^{\mathrm{T}}$. d is the positive parameter to be designed, $0 < d < 1$, and the presence of powers $1+d$ and $1-d$ can improve the speed at which the system state state variables reach the sliding mode surface and reduce jitter.

Theorem 1: For the error state equation of (32), if the sliding mode surface (33) and the improved double power reaching law (35) are selected, and the designed INFTSMO control law is (36), then error e converges in finite time. Taking the q-axis as an example, the convergence time t_s is (37)

$$\begin{cases} \mathbf{v} = \mathbf{v}_{eq} + \mathbf{v}_n \\ \mathbf{v}_{eq} = \mathbf{A}\mathbf{e} \\ \mathbf{v}_n = \int_0^t \begin{bmatrix} \mathbf{k}_2 \left|\mathbf{s}\right|^{1+d} \mathrm{sgn}(\mathbf{s}) + \mathbf{k}_1 \left(\left|\mathbf{x}\right| \left|\mathbf{s}\right|\right)^{1-d} \mathrm{sgn}(\mathbf{s}) \\ + \mathbf{a}\dot{\mathbf{e}}/(\mathbf{b} + p/q \cdot \mathbf{c}\dot{\mathbf{e}}^{p/q-1}) \end{bmatrix} d\tau \end{cases} \tag{36}$$

$$\begin{aligned} t_s &= \frac{1}{k_{2q} d} \sqrt{\frac{k_{2q}}{k_{1q} \left|x_q\right|^{1-d}}} \arctan\left(\sqrt{\frac{k_{2q}}{k_{1q} \left|x_q\right|^{1-d}}} \left|s_q\right|^d\right) \\ &< T_{\text{max}} = \frac{\pi}{2d_q \sqrt{k_{2q} k_{1q}}} \end{aligned} \tag{37}$$

where INFTSMO control law consists of $\mathbf{v}_n$ and $\boldsymbol{v}_q$. $\mathbf{v}_n$ is the switching control law that allows the state variables to quickly reach the sliding mode surface $\mathbf{s}$. $\mathbf{v}_{eq}$ is an equivalent control law that ensures the state variable continues to stay on the $\mathbf{s} = 0$ after reaching the $\mathbf{s}$.

Proof 1: The selected Lyapunov function V is as follows

$$V = \frac{1}{2}\mathbf{s}^2 \tag{38}$$

Taking the q-axis as an example, deriving (38) and substituting (35) into (38) yields

$$\begin{aligned} \dot{V} &= s_q \dot{s}_q = s_q \Big[-k_{1q} \left(\left|x_q\right| \left|s_q\right|\right)^{1-d} \\ &\quad \mathrm{sgn}\left(s_q\right) - k_{2q} \left|s_q\right|^{1+d} \mathrm{sgn}\left(s_q\right) \Big] \\ &= -k_{1q} \left(\left|x_q\right| \left|s_q\right|\right)^{2-d} - k_{2q} \left|s_q\right|^{2+d} \leqslant 0 \end{aligned} \tag{39}$$

When $s_q > 0$, the following expression can be obtained from (35) follows

$$\dot{s}_q + k_{1q} \left(\left|x_q\right| s_q\right)^{1-d} + k_{2q} s_q^{1+d} = 0 \tag{40}$$

Dividing both sides of (40) by s_q^{1-d} yields

$$\dot{s}_q s_q^{d-1} + k_{1q} \left|x_q\right|^{1-d} + k_{2q} s_q^{2d} = 0 \tag{41}$$

Let $\tau = s_q^{1-d}$, then (41) can be expressed as follows

$$\dot{\tau} + dk_{2q}\tau^2 + dk_{1q} \left|x_q\right|^{1-d} = 0 \tag{42}$$

Solving (42) yields the general solution as follows

$$\tau = \sqrt{\frac{k_{2q}}{k_{1q} \left|x_q\right|^{1-d}}} \tan\left(T_0 - dt\sqrt{k_{2q} k_{1q} \left|x_q\right|^{1-d}}\right) \tag{43}$$

From $s_q(0) = s_{q0}$, therefore $T_0 = \arctan(\sqrt{k_{1q}|x_q|^{1-d}/k_{2q}}$ $|s_{q0}|^d)$; then when $s_q(t) = 0$, t_s can be obtained from (42) and (43) as follows

$$t_s = \frac{1}{k_{2q} d} \sqrt{\frac{k_{2q}}{k_{1q} \left|x_q\right|^{1-d}}} \arctan\left(\sqrt{\frac{k_{2q}}{k_{1q} \left|x_q\right|^{1-d}}} \left|s_q\right|^d\right) \tag{44}$$

Since the value range of the arctan function is $(-\pi/2, \pi/2)$, when $|x_q| > 1$, the following inequality can be obtained as follows

$$t_s < T_{\text{max}} = \frac{\pi}{2d\sqrt{k_{2q} k_{1q}}} \tag{45}$$

Deriving (38) and substituting (34) into (38), the following expression is obtained

$$\begin{aligned} \dot{V} &= \mathbf{s}\dot{\mathbf{s}} = \mathbf{s}\left[\mathbf{a}\dot{\mathbf{e}} + \left(\mathbf{b} + \frac{p}{q}\mathbf{c}\dot{\mathbf{e}}^{p/q-1}\right)\ddot{\mathbf{e}}\right] \\ &= \mathbf{s}\left(\mathbf{b} + \frac{p}{q}\mathbf{c}\dot{\mathbf{e}}^{p/q-1}\right)\left(\ddot{\mathbf{e}} + \frac{\mathbf{a}\dot{\mathbf{e}}}{\mathbf{b} + p/q \cdot \mathbf{c}\dot{\mathbf{e}}^{p/q-1}}\right) \end{aligned} \tag{46}$$

Deriving (32) and substituting it into (46) yields

$$\begin{aligned} \dot{V} &= \mathbf{s}\left(\mathbf{b} + \frac{p}{q}\mathbf{c}\dot{\mathbf{e}}^{p/q-1}\right) \\ &\quad \left(\mathbf{A}\dot{\mathbf{e}} + \mathbf{C}\dot{\mathbf{d}} - \dot{\mathbf{v}} + \frac{\mathbf{a}\dot{\mathbf{e}}}{\mathbf{b} + p/q \cdot \mathbf{c}\dot{\mathbf{e}}^{p/q-1}}\right) \end{aligned} \tag{47}$$

Deriving (36) and substituting it into (47) yields

$$\begin{aligned} \dot{V} &= -\left(\mathbf{b} + \frac{p}{q}\mathbf{c}\dot{\mathbf{e}}^{p/q-1}\right) \\ &\quad \left(\mathbf{k}_2 \left|\mathbf{s}\right|^{2+d} + \left|\mathbf{s}\right| \left(\mathbf{k}_1 (\left|\mathbf{x}\right| \left|\mathbf{s}\right|)^{1-d} - \mathbf{C}\dot{\mathbf{d}}\right)\right) \end{aligned} \tag{48}$$

Equation (48) can also be represented as

$$\begin{aligned} \dot{V} &= -\left(\mathbf{b} + \frac{p}{q}\mathbf{c}\dot{\mathbf{e}}^{\frac{p}{q}-1}\right) \\ &\quad \left(\mathbf{k}_1 \left|\mathbf{x}\right|^{1-d} \left|\mathbf{s}\right|^{2-d} + \left|\mathbf{s}\right| \left(\mathbf{k}_2 \left|\mathbf{s}\right|^{1+d} - \mathbf{C}\dot{\mathbf{d}}\right)\right) \end{aligned} \tag{49}$$

Assuming that $\left|\mathbf{C}\dot{\mathbf{d}}\right|$ is bounded when $\mathbf{k}_1(|\mathbf{x}||\mathbf{s}|)^{1-d} - \left|\mathbf{C}\dot{\mathbf{d}}\right| \geq 0$, $\mathbf{k}_2|\mathbf{s}|^{1+d} - \left|\mathbf{C}\dot{\mathbf{d}}\right| \geq 0$, and $p/q > 1$, $\dot{\mathbf{e}}^{p/q-1} > 0$, $\mathbf{k}_1 > 0$, $\mathbf{k}_2 > 0$.

From (48) the following inequality can be obtained

$$\dot{V} \leq -\left(\mathbf{b} + \frac{p}{q} \cdot \mathbf{c}\dot{\mathbf{e}}^{p/q-1}\right)\left(\mathbf{k}_2 \left|\mathbf{s}\right|^{2+d}\right) \leq 0 \tag{50}$$

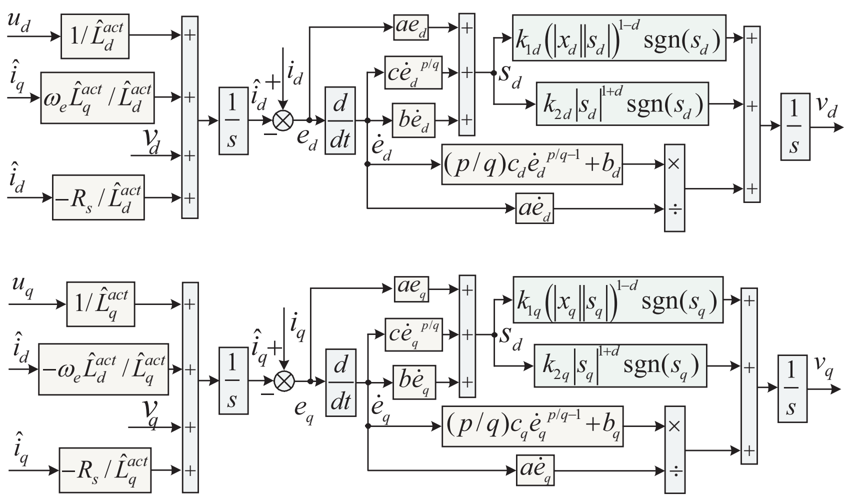

FIGURE 3. The block diagram of INFTSMO.

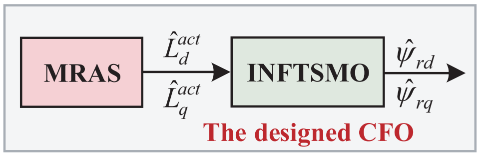

FIGURE 4. The schematic diagram of CFO.

From (49) the following inequality can be obtained

$$\dot{V} \le -\left(\mathbf{b}+\frac{p}{q}\cdot\mathbf{c}\dot{\mathbf{e}}^{p/q-1}\right)\left(\mathbf{k}_1\left|\mathbf{x}\right|^{1-d}\left|\mathbf{s}\right|^{2-d}\right)\le 0 \tag{51}$$

From (50) and (51), it can be seen that $\dot{V} \le 0$, and the state variables will reach the sliding mode surface in limited time.

In summary, the design steps for the CFO are as follows

1) The discrete MRAS is constructed from (21) and (22).
2) The d-q axis inductances are estimated from (29) and used as the input to (31).
3) According to (31), the INFTSMO is constructed, which is ultimately cascaded with discrete MRAS to form a CFO for real-time observation of the PM flux linkage.

The block diagram of INFTSMO is shown in Fig. 3, and the schematic diagram of CFO is shown in Fig. 4.

From (31), the predicted current value for the next moment observed by INFTSMO is as follows

$$\begin{cases} \hat{i}_d(k+1)=\left(1-\frac{R_sT_s}{\hat{L}_d^{act}}\right)\hat{i}_d(k) \\ +\frac{T_s\omega_e(k)\hat{L}_q^{act}}{\hat{L}_d^{act}}\hat{i}_q(k)+\frac{T_s}{\hat{L}_d^{act}}u_d(k)+\frac{\omega_e(k)T_s}{\hat{L}_d^{act}}\hat{\psi}_{rq} \\ \hat{i}_q(k+1)=\left(1-\frac{R_sT_s}{\hat{L}_q^{act}}\right)\hat{i}_q(k)-\frac{T_s\omega_e(k)\hat{L}_d^{act}}{\hat{L}_q^{act}}\hat{i}_d(k) \\ +\frac{T_s}{\hat{L}_q^{act}}u_q(k)-\frac{\omega_e(k)T_s}{\hat{L}_q^{act}}\hat{\psi}_{rd} \end{cases} \tag{52}$$

where $\hat{i}_d$ and $\hat{i}_q$ are the observed value of d-q axis currents respectively.

5. DESIGN OF RDFTPCC STRATEGY

When $i_d = 0$ control is adopted, and it can be shown from (3) that the PM flux linkage is a reverse ratio to i_q in the case of certain electromagnetic torque. When the IPMSM is demagnetized, it will inevitably cause a sudden increase in i_q. However, the output capacity of the inverter is limited, and i_q will reach its limit value. At this time, it is no longer possible to compensate for the missing electromagnetic torque by adjusting i_q, and it can only be achieved by adjusting i_d.

When the motor suffers from inductance mismatch and demagnetization fault, (5) can be rewritten as

$$\begin{cases} \psi_d=\psi_{rd}+L_d^{act}i_d=\psi_{ext}^F+L_q^{act}i_d \\ \psi_q=\psi_{rq}+L_q^{act}i_q \end{cases} \tag{53}$$

where $\psi_{ext}^F=\psi_{rd}+(L_d^{act}-L_q^{act})i_d$ is the effective flux linkage of the motor after PM demagnetization and inductance mismatch.

Substituting (53) into (1) and performing the forward first-order Eulerian discretization, the d-axis stator flux at the next moment is obtained as follows

$$\psi_d(k+1) = \left(1-T_s\frac{R_s}{L_q^{act}}\right)\psi_d(k)+T_s\omega_e(k)\psi_q(k)$$

$$+T_su_d(k)+T_s\frac{R_s}{L_q^{act}}\psi_{ext}^F(k) \tag{54}$$

A first-order forward Eulerian discretization of (53) and the flux equation at moment $k+1$ can be further expressed as

$$\begin{cases} \psi_d(k+1) = \psi_{ext}^F(k+1) + L_q^{act} i_d^{ref}(k+1) \\ \psi_q(k+1) = \psi_{rq}(k+1) + L_q^{act} i_q(k+1) \end{cases} \tag{55}$$

where $i_d^{ref}(k+1)$ is the d-axis reference current at the next time.

Substituting (55) into (54), the effective flux linkage at moment $k+1$ is

$$\begin{aligned} \psi_{ext}^F(k+1) = \psi_{ext}^F(k) + \left(1 - T_s \frac{R_s}{L_q^{act}}\right) L_q^{act} i_d(k) \\ + T_s \omega_e(k) \psi_{rq} + T_s \omega_e(k) L_q^{act} i_q(k) \\ + T_s u_d(k) - L_q^{act} i_d^{ref}(k+1) \end{aligned} \tag{56}$$

Using the theory of deadbeat control, let the effective flux linkage at moment $k+1$ equal to a suitable value Ψ, (56) is rewritten as

$$\begin{aligned} \Psi \;=\; \psi_{ext}^F(k) + \left(1 - T_s \frac{R_s}{L_q^{act}}\right) L_q^{act} i_d(k) \\ + T_s \omega_e(k) \psi_{rq} + T_s \omega_e(k) L_q^{act} i_q(k) \\ + T_s u_d(k) - L_q^{act} i_d^{ref}(k+1) \end{aligned} \tag{57}$$

This paper adopts control with $i_d = 0$. From (4), the effective flux linkage of IPMSM without demagnetization is

$$\psi_{ext} = \psi_{ro} \tag{58}$$

Let the electromagnetic torque before and after the demagnetization fault be equal, and we can obtain

$$\frac{3}{2} n_p [\Psi i_q(k+1) - \psi_{rq} i_d(k+1)] = \frac{3}{2} n_p \psi_{ro} i_q(k) \tag{59}$$

Therefore, from (59) Ψ can be denoted as

$$\Psi = \frac{\psi_{ro} i_q(k) + \psi_{rq} i_d(k+1)}{i_q(k+1)} \tag{60}$$

To quickly restore i_q after demagnetization to its value of the normal operation of the motor, let

$$i_q(k+1) = i_q(k) \tag{61}$$

Substituting (61) into (60), the following expression is obtained

$$\Psi = \psi_{ro} + \frac{\psi_{rq} i_d(k+1)}{i_q(k+1)} \tag{62}$$

Substituting (62) into (57) and replacing the d-q axis flux linkage component, d-q axis inductances, and d-q axis current at $k+1$ with the observed values, the $i_d^{ref}(k+1)$ is

$$\begin{aligned} i_d^{ref}(k+1) = \frac{1}{\hat{L}_q^{act}} \left[\psi_{ext}^F(k) - \left[\psi_{ro} + \frac{\hat{\psi}_{rq} \hat{i}_d(k+1)}{\hat{i}_q(k+1)} \right] \right] \\ + \left(1 - \frac{R_s}{\hat{L}_q^{act}} T_s\right) i_d(k) \\ + \frac{T_s}{\hat{L}_q^{act}} \left[\omega_e(k) \hat{L}_q^{act} i_q(k) + u_d(k) + \omega_e(k) \hat{\psi}_{rq} \right] \end{aligned} \tag{63}$$

When IPMSM operates normally, $\psi_{rq} = 0$, $\psi_{ext}^F(k) = \psi_{ro}$, and from (63), $i_d^{ref}(k+1) = 0$. Therefore, the system still adopts the control strategy of $i_d = 0$. When demagnetization fault occurs in the motor, $\psi_{rq} \neq 0$, $\psi_{ext}^F(k) \neq \psi_{ro}$. At this point, it is necessary to adjust the $i_d^{ref}(k+1)$ calculated by (63) to compensate for the torque loss caused by demagnetization.

In addition, due to the limited output capacity of the inverter, $i_d^{ref}(k+1)$ needs to satisfy the following constraint

$$i_d^{ref}(k+1) > -\sqrt{i_{s\,\max}^2 - i_q^2} \tag{64}$$

The control system of a conventional DPCC has a delay the reference voltage $u^*(k)$ is output by the inverter at the moment $k+1$, resulting in a one-beat delay in the control voltage. To make the system control performance as unaffected as possible by the delay, $\hat{i}(k+1)$ should be used instead of the sampling current $i(k)$.

In summary, replacing the $i_d^*(k+1)$ in (10) with the $i_d^{ref}(k+1)$ in (63), and replacing the inductance, flux linkage and current with the observed values, the desired voltage output by the proposed RDFTPCC is shown in (65).

$$\begin{cases} u_d^*(k) = \hat{L}_d^{act} \frac{i_d^{ref}(k+1) - \hat{i}_d(k+1)}{T_s} \\ -\omega_e(k) \hat{L}_q^{act} i_q(k) + R_s i_d(k) - \omega_e(k) \hat{\psi}_{rq} \\ u_q^*(k) = \hat{L}_q^{act} \frac{i_q^*(k+1) - \hat{i}_q(k+1)}{T_s} \\ +\omega_e(k) \hat{L}_d^{act} i_d(k) + R_s i_q(k) + \omega_e(k) \hat{\psi}_{rd} \end{cases} \tag{65}$$

In addition, since $L_d = L_q$ in the surface permanent magnet synchronous motor (SPMSM), $(L_d^{act} - L_q^{act}) i_d = 0$. It is not possible to compensate the missing torque by adjusting its i_d; therefore, the proposed RDFTPCC method is not applicable to SPMSM. The flowchart of RDFTPCC is shown in Fig. 5, and the system block diagram of CFO-based RDFTPCC is shown in Fig. 6.

6. EXPERIMENTAL RESULTS AND ANALYSIS

Since the demagnetization fault of IPMSM is difficult to simulate on real motors, to verify the feasibility and validity of the proposed algorithm, RT-LAB is used to establish the hardware in the loop simulation experiment (HILS) platform, as shown in Fig. 7. The DSP adopts TMS320F2812, and IPMSM demagnetization fault and parameter mismatch are reconstructed by RT-LAB (OP5600).

In this paper, $i_d = 0$ control method is adopted. The parameters of IPMSM are given in Table 1, and the parameters of the control system are given in Table 2. In addition, the parameter θ of the designed discrete MRAS is set to 0.0001. The experimental results of the proposed RDFTPCC-CFO method are compared with DPCC, RDFTPCC-SMO, and RDFTPCC-INFTSMO methods.

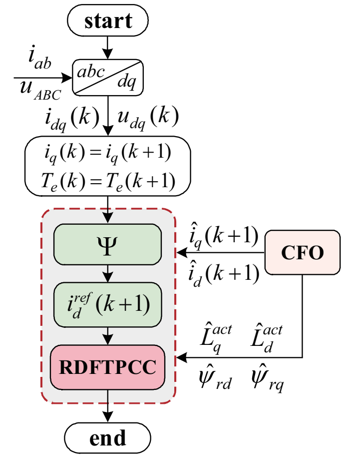

FIGURE 5. The flowchart of RDFTPCC.

TABLE 1. Parameters of IPMSM.

Parameters	Values
Number of pole pairs (n_p)	4
Stator resistance (R_s)	0.02 Ω
q-axis inductance (L_q)	0.003572 H
d-axis inductance (L_d)	0.0015 H
PM flux linkage (ψ_{ro})	0.892 Wb
DC voltage (U_{dc})	1500 V
Rotational inertia (J)	1 kg · m^2
Viscous friction coefficient (B)	0.001 Nm · s/rad

TABLE 2. The parameters of the control system.

SMO	INFTSMO
$k_d = 50000$	$a = 200$
$k_q = 50000$	b =0.2
-	$c = 0.01$
-	$p/q = 7/5$
-	$k_1 = 5000$
-	$k_2 = 5000$
-	$d = 0.33$

6.1. Performance Comparison of Control Methods for PM Demagnetization

The working conditions are set as follows: The motor starts with no load, and the reference speed N_r^{ref} is 300 r/min. At 0.2 s, the load torque T_L is loaded from 0 to 650 N · m. At 0.5 s; the IPMSM is demagnetized; and the amplitude of the PM flux linkage decreases from $\psi_{ro} = 0.892$ Wb to $\psi_r = 0.6$ Wb, while the magnetic deviation angle γ changes from 0 to $\pi/6$ rad. At 0.7 s, T_L is loaded from 650 to 700 N · m. The total running time is 1 s.

Figures 8, 9, 10, 11, and 12 show the experimental waveforms of four methods for IPMSM PM demagnetization, respectively. Among them, Figs. 8, 9, and 10 show the d-q axis current, electromagnetic torque, and speed waveforms for the four methods, respectively. Fig. 11 shows the d-axis reference current waveforms for the RDFTPCC-SMO, RDFTPCC-INFTSMO, and RDFTPCC-CFO methods, respectively. Figs. 12(a), (b), and (c) show the observed waveforms of the d-q axis flux linkage and the identified waveforms of the d-q-axis inductances, respectively.

The experimental waveforms after 0.5 s PM demagnetization are analyzed as follows.

From Figs. 8 to 10, at 650 N · m load torque, the i_q of the DPCC rapidly increases to the limit value of 200 A, and its T_e is only 620 N · m, which is less than the load torque. This results in a substantial decrease in speed. Compared with the DPCC, the i_q of the other three methods do not increase abruptly to the limit value, and they all quickly return to the steady state value of 122 A after a small fluctuation. T_e can always be maintained at 650 N · m. Therefore, their speeds can quickly and accurately track the given speed. When the load torque abruptly changes from 650 to 700 N · m, the T_e of the other three methods can still reach and maintain 700 N · m, and their speeds remain normal, so the proposed RDFTPCC method can drive a larger load when the permanent magnet is demagnetized.

From Fig. 11, compared with the DPCC, the remaining three methods can output $i_d^{ref}(k+1)$ to compensate for missing torque. At 650 N · m load torque, the theoretical calculated and constrained values of $i_d^{ref}(k+1)$ are -82.1 A and -158.4 A, respectively. At 700 N · m load torque, the theoretical calculated and constrained values of $i_d^{ref}(k+1)$ are -85.1 A and -150.69 A, respectively. The outputs of i_d and $i_d^{ref}(k+1)$ from the three methods are consistent with the theoretical values within the constraint range.

From Fig. 12, CFO can quickly and accurately identify L_d and L_q, and since there is no flux linkage parameters in the designed MRAS, the demagnetization of PM has hardly any effect on the identification of inductance, demonstrating strong robustness. Whether during normal motor operation or in the event of demagnetization fault, the CFO can achieve the same accuracy of flux linkage observation as INFTSMO. The observation accuracy is higher than SMO, and the waveform jitter is smaller than SMO.

In summary, compared to the conventional DPCC, the remaining three methods are able to compensate the torque deficit caused by PM demagnetization in the motor and have stronger fault-tolerance. The i_d, i_q, T_e, speed, and $i_d^{ref}(k+1)$ of the proposed RDFTPCC-CFO method are not affected by the inductance identification, and the waveforms are still stable. When the motor is demagnetized, the same control effect as the RDFTPCC-INFTSMO method can be achieved, both better than the RDFTPCC-SMO method. Compared with SMO and INFTSMO, the MRAS in the proposed CFO can accurately identify the L_d and L_q when the motor is demagnetized and quickly input it into INFTSMO, thus realizing the accurate observation of the PM flux linkage. There is no issue of failure in detecting demagnetization fault caused by inaccurate inductance identification.

6.2. Performance Comparison of Control Methods for PM Demagnetization and Inductance Mismatch

The working conditions are set as follows: the motor starts with no load and N_r^{ref} is 300 r/min. At 0.2 s, T_L is loaded from 0 to

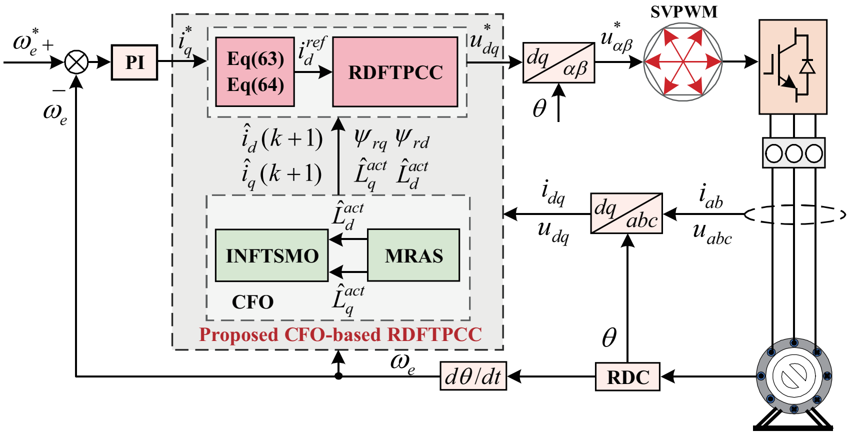

FIGURE 6. The system block diagram of CFO-based RDFTPCC.

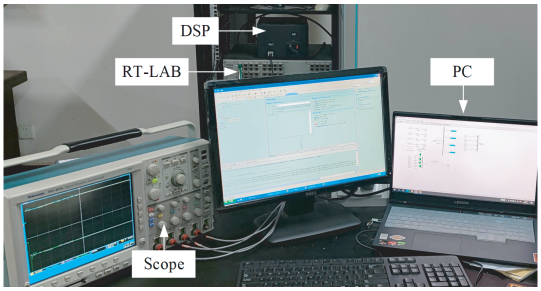

FIGURE 7. RT-LAB experiment platform.

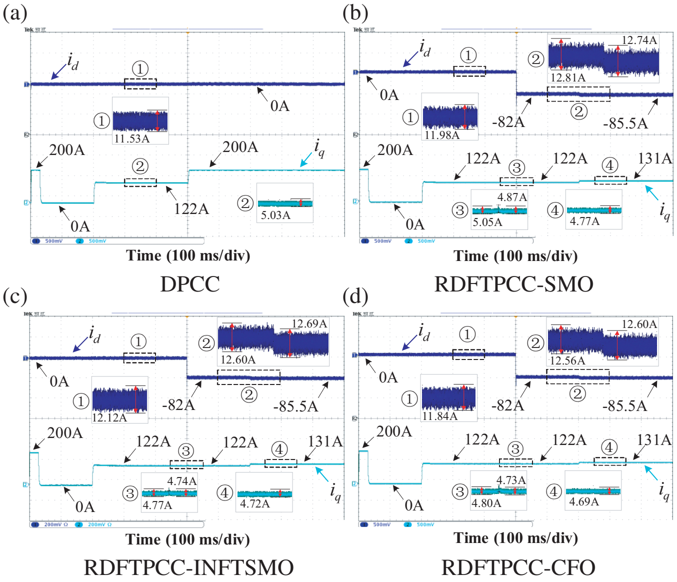

DPCC
RDFTPCC-SMO
RDFTPCC-INFTSMO
RDFTPCC-CFO

FIGURE 8. The waveforms of the d-q axis current.

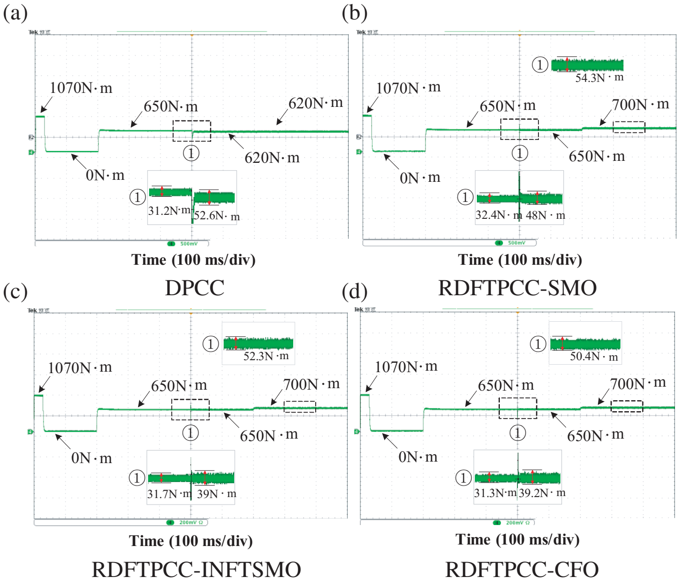

DPCC
RDFTPCC-SMO
RDFTPCC-INFTSMO
RDFTPCC-CFO

FIGURE 9. The electromagnetic torque waveforms.

650 N · m. At 0.55 s, the IPMSM is demagnetized, and the amplitude of the PM flux linkage decreases from $\psi_{ro} = 0.892$ Wb to $\psi_r = 0.6$ Wb, while the magnetic deviation angle γ changes from 0 to $\pi/6$ rad. At 0.9 s, L_d and L_q decrease to 0.5 times of the nominal value. At 1.25 s, L_d and L_q increase to 1.5 times of the nominal value. At 1.6 s, T_L is loaded from 650 to 700 N · m. The total running time is 2 s.

Figures 13, 14, 15, 16, and 17 show the experimental waveforms of four methods for PM demagnetization and inductance mismatch, respectively. Among them, Figs. 13, 14, and 15 show the d-q axis current, electromagnetic torque, and speed waveforms for the four methods, respectively. Fig. 16 shows the d-axis reference current waveforms for the RDFTPCC-SMO, RDFTPCC-INFTSMO, and RDFTPCC-CFO methods, respectively. Figs. 17(a), (b), and (c) show the observed waveforms of the d-q axis flux linkage and the identified waveforms of the d-q-axis inductances, respectively.

Before 0.9 s, the IPMSM only experiences the process from normal operation to demagnetization fault. Therefore, the experimental results in Figs. 13, 14, 15, 16, and 17 are all the same as those in Figs. 8, 9, 10, 11, and 12.

The experimental waveforms after 0.9 s inductance mismatch are analyzed as follows.

From Figs. 13 to 15, at 650 N · m load torque, the T_e of the DPCC method remains at 620 N · m, so the speed of the DPCC method cannot track the given speed. The i_q, T_e, and speed waveform jitter of the RDFTPCC-SMO and RDFTPCC-INFTSMO methods are serious and abnormal. However, the i_q, T_e, and speed waveforms of the RDFTPCC-CFO method are smoother and more stable. When the load torque abruptly changes from 650 to 700 N · m, the i_q, T_e, and speed waveforms of the RDFTPCC-CFO method can remain smooth and stable. The results indicate that the RDFTPCC-CFO method fully suppresses the effect of inductance mismatch.

From Fig. 16, at 650 N · m load torque, when the inductance decreases and increases, the theoretical calculated values of $i_d^{ref}(k+1)$ are -106.5 A and -66.9 A, respectively. At 700 N · m load torque, when the inductance increases, the the-

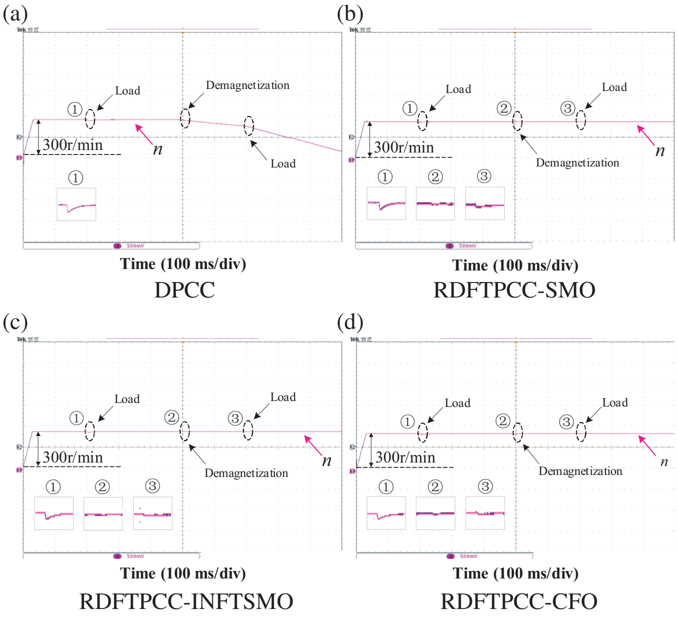

DPCC

RDFTPCC-SMO

RDFTPCC-INFTSMO

RDFTPCC-CFO

FIGURE 10. The speed waveforms.

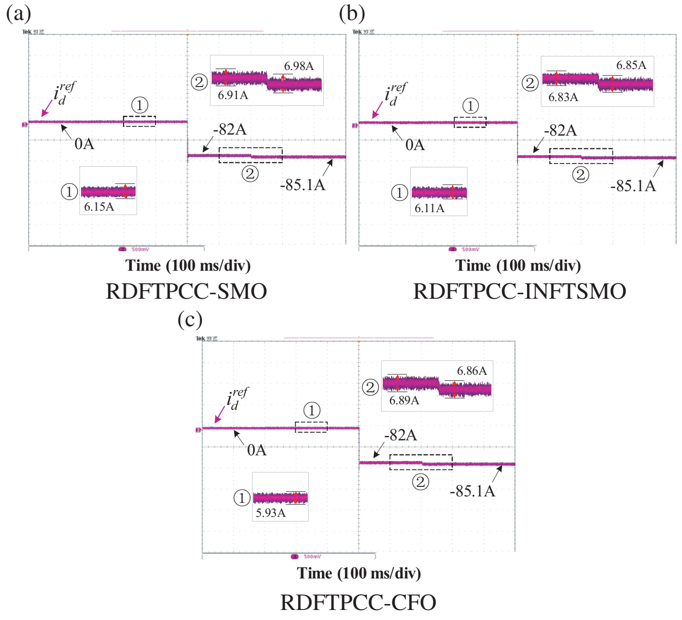

RDFTPCC-SMO

RDFTPCC-INFTSMO

RDFTPCC-CFO

FIGURE 11. The speed waveforms.

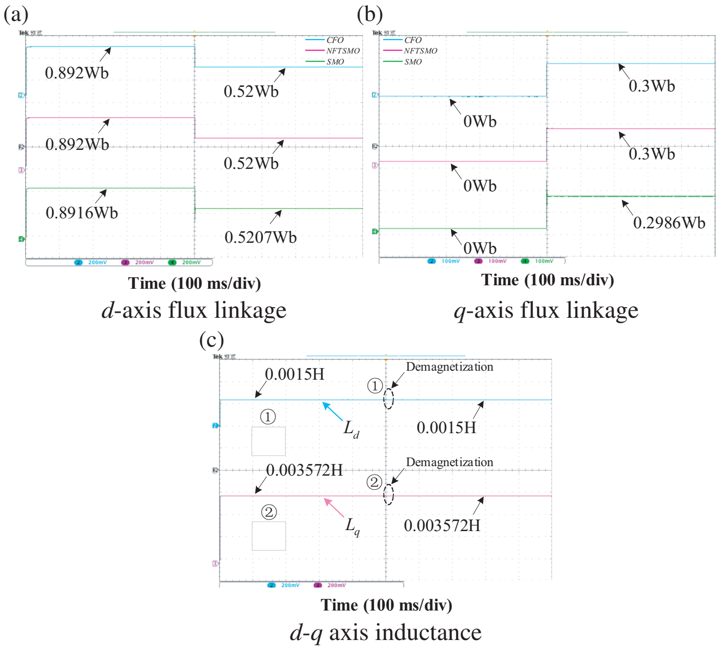

d-axis flux linkage

q-axis flux linkage

d-q axis inductance

FIGURE 12. The identified waveforms.

oretical calculated value of $i_d^{ref}(k+1)$ is -68.9 A. The i_d and $i_d^{ref}(k+1)$ of RDFTPCC-SMO and RDFTPCC-INFTSMO have significant deviations from the theoretical calculated values, and the waveforms have obvious jitter. However, the $i_d^{ref}(k+1)$ in the proposed RDFTPCC-CFO can still be accurately calculated, and the waveform is more stable.

The comprehensive performance comparison of control methods for PM demagnetization and inductance mismatch is shown in Table 3.

From Fig. 17, when the IPMSM suffers from both demagnetization fault and inductance mismatch, the demagnetization fault detection capabilities of SMO and INFTSMO both fail, and the waveform jitter is serious. However, the designed CFO can still quickly and accurately identify the actual L_d and L_q, thus realizing the accurate detection of the demagnetization fault, which greatly improves the fault tolerance and robustness of the system.

The performance comparison of the flux linkage observer is shown in Table 4.

Figure 18 shows the THD of the A-phase stator current for the RDFTPCC-SMO, RDFTPCC-INFTSMO, and RDFTPCC-CFO methods. Between 1.25 s and 1.6 s, the PM demagne-

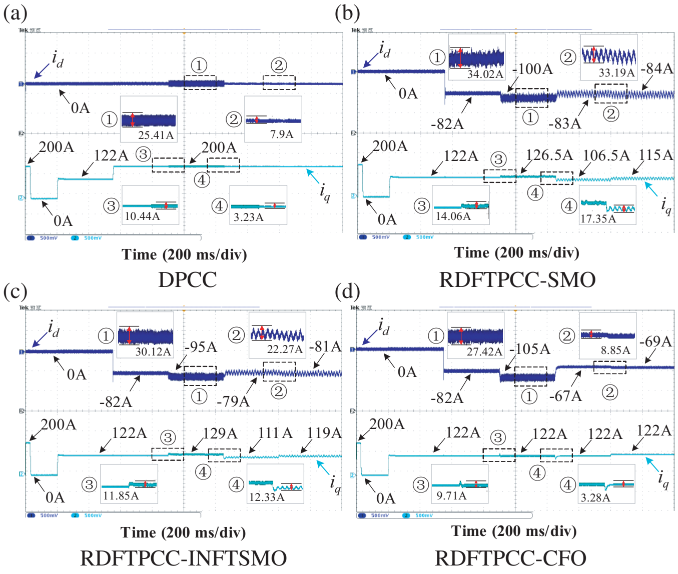

FIGURE 13. The the d-q axis current waveforms.

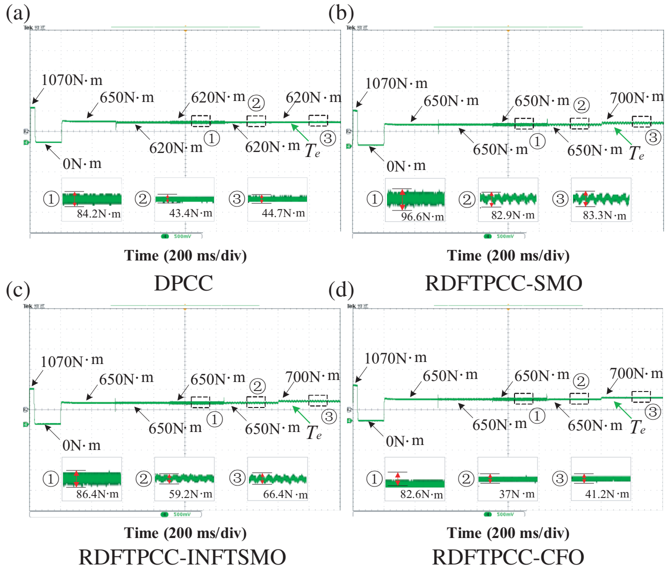

FIGURE 14. The electromagnetic torque waveforms.

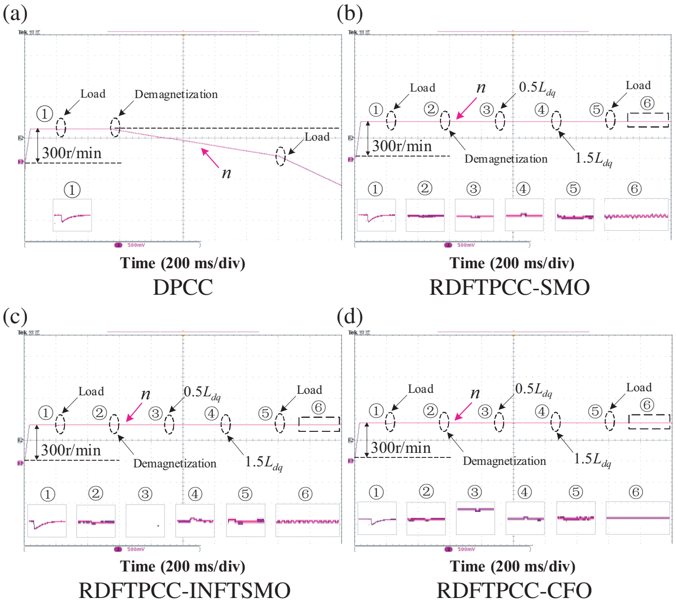

FIGURE 15. The speed waveforms.

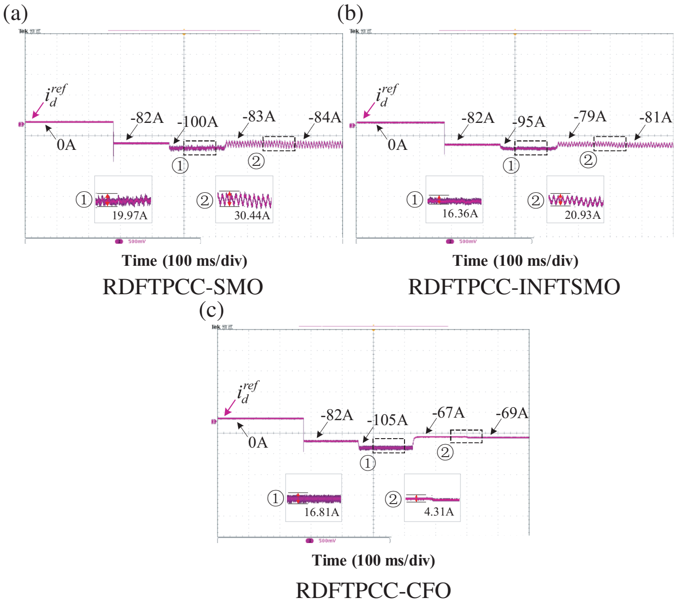

FIGURE 16. The speed waveforms.

TABLE 3. The comprehensive performance comparison of control methods for PM demagnetization and inductance mismatch.

Performance indicators	Methods	Values (%)
Speed ripple	RDFTPCC-SMO	0.065/0.155
	RDFTPCCINFTSMO	0.04/0.096
	RDFTPCCCFO	0.01/0.006
Torque ripple	RDFTPCC-SMO	7.42/6.38
	RDFTPCCINFTSMO	6.65/4.55
	RDFTPCCCFO	6.35/2.84

Remark 1: I/II are the values obtained for the motor in the following two states: I. PM demagnetization and inductance decrease to 0.5 times the nominal value. II. PM demagnetization and inductance increase to 1.5 times the nominal value.

tization and inductance mismatch occur simultaneously. By analyzing the waveforms in this interval, it is known that the THDs of the RDFTPCC-SMO, RDFTPCC-INFTSMO, and RDFTPCC-CFO are 5.90%, 4.05% and 1.29%, respectively. The results indicate that the proposed RDFTPCC-CFO method can effectively suppress current harmonics during PM demagnetization and inductor mismatch.

In summary, when the demagnetization fault and inductance mismatch occur simultaneously in a motor, compared with the DPCC, RDFTPCC-SMO, and RDFTPCC-INFTSMO methods, the proposed RDFTPCC-CFO reduces the impact of inductance mismatch on demagnetization fault detection and fault-tolerant control. Moreover, the MRAS in the proposed CFO can accurately identify the actual L_d and L_q, and quickly feed back to INFTSMO, realizing the accurate demagnetization fault detec-

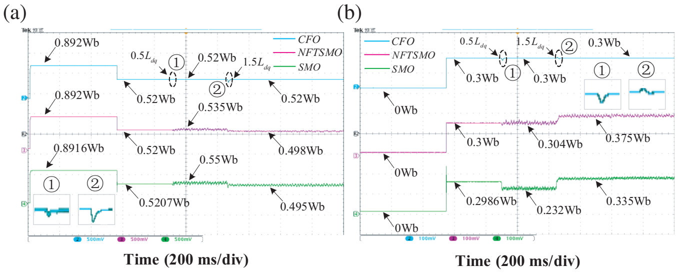

d-axis flux linkage *q*-axis flux linkage

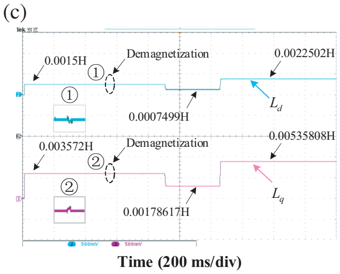

d-*q* axis inductance

FIGURE 17. The identified waveforms.

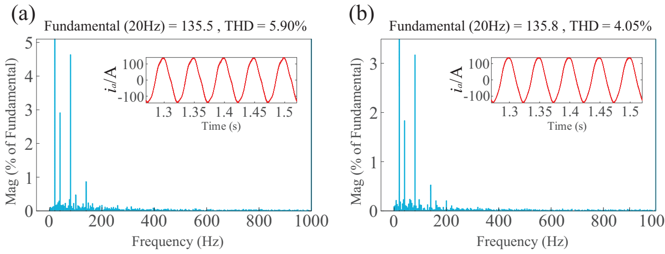

RDFTPCC-SMO RDFTPCC-INFTSMO

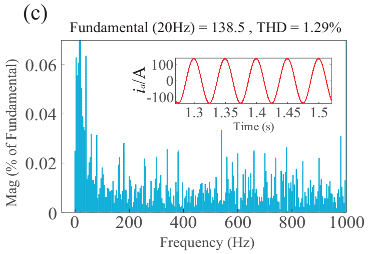

RDFTPCC-CFO

FIGURE 18. THD analysis of A phase stator current.

TABLE 4. The performance comparison of the flux linkage observers.

Parameters	Observers	Flux linkage steady state values (Wb)
ψ_{rd}	SMO	0.8916/0.5207/0.55/0.495
	INFTSMO	0.892/0.52/0.535/0.498
	CFO	0.892/0.52/0.52/0.52
ψ_{rq}	SMO	0/0.2986/0.232/0.335
	INFTSMO	0/0.3/0.304/0.375
	CFO	0/0.3/0.3/0.3

Remark 2: I/II/III/IV are the values obtained for the motor in the following four states: I. Normal operation. II. PM demagnetization. III. PM demagnetization and inductances decrease to 0.5 times the nominal value. IV. PM demagnetization and inductances increase to 1.5 times the nominal value.

tion, and the impact of parameter mismatch on control performance is reduced. Therefore, the waveforms are smoother; the harmonics are suppressed; and the system stability is effectively improved, with stronger fault tolerance and robustness.

7. CONCLUSION

An RDFTPCC method based on CFO is proposed, which reduces the impact of inductive mismatch on the demagnetization fault detection and fault-tolerant control, effectively compensates for the torque loss caused by the demagnetization fault and the control performance degradation due to parameter mismatch. The fault-tolerance capability and robustness of the system have been further enhanced. Through the experimental analysis of different operating conditions, the following main conclusions can be obtained:

(1) In comparison to the conventional DPCC method, $i_d^{ref}(k+1)$ can be timely output by the proposed RDFTPCC after demagnetization fault occurs in the motor, and the missing torque is effectively compensated, with stronger fault-tolerance.

(2) Compared with the RDFTPCC-SMO and RDFTPCC-INFTSMO methods, when inductance mismatch occurs, the CFO in the proposed RDFTPCC-CFO can accurately detect demagnetization fault and identify the actual d-q axis inductance, which reduces the impact of the parameter mismatch; therefore, $i_d^{ref}(k+1)$ can be more accurately output, with greater robustness.

(3) In contrast to the RDFTPCC-SMO and RDFTPCC-INFTSMO methods, when PM demagnetization and inductance mismatch occur simultaneously, the speed pulsations of the RDFTPCC-CFO are in average reduced by 92.7% and 88.2%; the torque ripples are in average suppressed by 33.40% and 17.95%; the THD is decreased by 78.1% and 68.1%; and the stability of the system is further enhanced.

ACKNOWLEDGEMENT

This work was supported by the Scientific Research Fund of Hunan Provincial Education Department under Grant Number 23B1017.

REFERENCES

[1] Feng, G., C. Lai, X. Tan, W. Peng, and N. C. Kar, "Multiparameter estimation of PMSM using differential model with core loss compensation," *IEEE Transactions on Transportation Electrification*, Vol. 8, No. 1, 1105–1115, 2022.

[2] Dong, Q., B. Wang, Y. Yu, M. Tian, and D. Xu, "A rotor position estimation scheme using inherent excitation source for finite-control set model predictive control in low-speed region," *IEEE Transactions on Industrial Electronics*, 2024.

[3] Boldea, I., L. N. Tutelea, W. Xu, and M. Pucci, "Linear electric machines, drives, and MAGLEVs: An overview," *IEEE Transactions on Industrial Electronics*, Vol. 65, No. 9, 7504–7515, 2018.

[4] Türker, T., U. Buyukkeles, and A. F. Bakan, "A robust predictive current controller for PMSM drives," *IEEE Transactions on Industrial Electronics*, Vol. 63, No. 6, 3906–3914, 2016.

[5] Jung, J.-W., V. Q. Leu, T. D. Do, E.-K. Kim, and H. H. Choi, "Adaptive PID speed control design for permanent magnet synchronous motor drives," *IEEE Transactions on Power Electronics*, Vol. 30, No. 2, 900–908, 2015.

[6] Ke, D., F. Wang, X. Yu, S. A. Davari, and R. Kennel, "Predictive error model-based enhanced observer for PMSM deadbeat control systems," *IEEE Transactions on Industrial Electronics*, Vol. 71, No. 3, 2242–2252, 2024.

[7] Bai, C., Z. Yin, Y. Zhang, and J. Liu, "Robust predictive control for linear permanent magnet synchronous motor drives based on an augmented internal model disturbance observer," *IEEE Transactions on Industrial Electronics*, Vol. 69, No. 10, 9771–9782, 2022.

[8] Dai, S., J. B. Wang, Z. Sun, and E. Chong, "Deadbeat predictive current control for high-speed PMSM drives with low switching-to-fundamental frequency ratios," *IEEE Transactions on Industrial Electronics*, Vol. 69, No. 5, 4510–4521, 2022.

[9] Xiao, S. and A. Griffo, "Pwm-based flux linkage and rotor temperature estimations for permanent magnet synchronous machines," *IEEE Transactions on Power Electronics*, Vol. 35, No. 6, 6061–6069, 2020.

[10] Huang, G., J. Li, E. F. Fukushima, C. Zhang, J. He, and K. Zhao, "An improved equivalent-input-disturbance approach for PMSM drive with demagnetization fault," *ISA Transactions*, Vol. 105, 120–128, 2020.

[11] Faiz, J. and E. Mazaheri-Tehrani, "Demagnetization modeling and fault diagnosing techniques in permanent magnet machines under stationary and nonstationary conditions: An overview," *IEEE Transactions on Industry Applications*, Vol. 53, No. 3, 2772–2785, 2017.

[12] Kakosimos, P. and H. Abu-Rub, "Deadbeat predictive control for PMSM drives with 3-L NPC inverter accounting for saturation effects," *IEEE Journal of Emerging and Selected Topics in Power Electronics*, Vol. 6, No. 4, 1671–1680, 2018.

[13] Espinosa, A. G., J. A. Rosero, J. Cusidó, L. Romeral, and J. A. Ortega, "Fault detection by means of Hilbert-Huang transform of the stator current in a PMSM with demagnetization," *IEEE Transactions on Energy Conversion*, Vol. 25, No. 2, 312–318, 2010.

[14] Ruiz, J.-R. R., J. A. Rosero, A. G. Espinosa, and L. Romeral, "Detection of demagnetization faults in permanent-magnet synchronous motors under nonstationary conditions," *IEEE Transactions on Magnetics*, Vol. 45, No. 7, 2961–2969, Jul. 2009.

[15] Akar, M. and M. Eker, "Demagnetization fault diagnosis in permanent magnet synchronous motors," *Przegląd Elektrotechniczny*, Vol. 89, No. 2a, 229–233, 2013.

[16] Eker, M. and B. Gündogan, "Demagnetization fault detection of permanent magnet synchronous motor with convolutional neural network," *Electrical Engineering*, Vol. 105, 1695–1708, 2023.

[17] Shi, Y., K. Sun, L. Huang, and Y. Li, "Online identification of permanent magnet flux based on extended Kalman filter for IPMSM drive with position sensorless control," *IEEE Transactions on Industrial Electronics*, Vol. 59, No. 11, 4169–4178, 2012.

[18] Xiao, X., C. Chen, and M. Zhang, "Dynamic permanent magnet flux estimation of permanent magnet synchronous machines," *IEEE Transactions on Applied Superconductivity*, Vol. 20, No. 3, 1085–1088, 2010.

[19] Zhao, J., L. Wang, L. Xu, F. Dong, J. Song, and X. Yang, "Uniform demagnetization diagnosis for permanent-magnet synchronous linear motor using a sliding-mode velocity controller and an aln-mras flux observer," *IEEE Transactions on Industrial Electronics*, Vol. 69, No. 1, 890–899, 2022.

[20] He, J., C. Zhang, S. Mao, H. Wu, and K. Zhao, "Demagnetization fault detection in permanent magnet synchronous motors based on sliding observer," *Journal Nonlinear Sciences and Applications*, Vol. 9, No. 5, 2039–2048, 2016.

[21] Zhang, C., M. Zhang, F. Zhang, and J. H. P. Wu, "A cascade observer to detect demagnetization faults for PMSM," *Electric Machines and Control*, Vol. 21, No. 2, 45–54, 2017.

[22] Luo, B., S. Peng, Y. Zhang, Z. Liu, and B. Huang, "A fault-tolerant control strategy for D-PMSG wind power generation system," *Progress In Electromagnetics Research C*, Vol. 123, 75–89, 2022.

[23] Zhao, K., Y. Chen, C. Zhang, J. He, G. Huang, and T. Li, "Finite-set model predictive fault control for demagnetization faults of permanent magnet synchronous motor drives," *Journal of Electronic Measurement and Instrument*, Vol. 33, No. 7, 79–87, 2019.

[24] Zhao, K., R. Zhou, A. Leng, and W. Dai, "Finite control set model-free fault-tolerant predictive control for permanent magnet synchronous motor," *Transactions of China Electrotechnical Society*, Vol. 36, No. 1, 27–38, 2021.

[25] Zhang, C., G. Wu, J. He, and K. Zhao, "Sliding observer-based demagnetisation fault-tolerant control in permanent magnet synchronous motors," *The Journal of Engineering*, Vol. 2017, No. 6, 175–183, 2017.

[26] Verkroost, L., J. D. Bisschop, H. Vansompel, F. D. Belie, and P. Sergeant, "Active demagnetization fault compensation for axial flux permanent-magnet synchronous machines using an analytical inverse model," *IEEE Transactions on Energy Conversion*, Vol. 35, No. 2, 591–599, 2020.

[27] Zhang, X., R. Tao, X. Xu, T. Wang, and H. Zhang, "Predictive current control of a PMSM three-level dual-vector model based on self-anti-disturbance techniques," *Journal of Electrical Engineering & Technology*, Vol. 17, No. 6, 3375–3388, 2022.

[28] Boldea, I., M. C. Paicu, and G.-D. Andreescu, "Active flux concept for motion-sensorless unified ac drives," *IEEE Transactions on Power Electronics*, Vol. 23, No. 5, 2612–2618, 2008.

[29] Zhao, K., A. Leng, R. Zhou, W. Dai, S. Wu, and T. Li, "Demagnetization fault reconstruction for six-phase permanent magnet synchronous motor by improved super-twisting algorithm-based sliding-mode observer," *Measurement*, Vol. 172, 108905, 2021.

[30] Li, H., J. Shao, and Z. Liu, "Incremental model predictive current control for PMSM with online compensation for parameter mismatch," *IEEE Transactions on Energy Conversion*, Vol. 38, No. 2, 1050–1059, 2023.

[31] Zhang, C., G. Wu, F. Rong, J. Feng, L. Jia, J. He, and S. Huang, "Robust fault-tolerant predictive current control for permanent magnet synchronous motors considering demagnetization fault," *IEEE Transactions on Industrial Electronics*, Vol. 65, No. 7, 5324–5334, 2018.

[32] Sun, X., M. Wu, G. Lei, Y. Guo, and J. Zhu, "An improved model predictive current control for PMSM drives based on current track circle," *IEEE Transactions on Industrial Electronics*, Vol. 68, No. 5, 3782–3793, 2021.

[33] Siami, M., D. A. Khaburi, and J. Rodríguez, "Torque ripple reduction of predictive torque control for PMSM drives with parameter mismatch," *IEEE Transactions on Power Electronics*, Vol. 32, No. 9, 7160–7168, 2017.

[34] Dugard, L. and I. D. Landau, "Convergence analysis of MRAS schemes used for recursive identification," *IFAC Proceedings Volumes*, Vol. 12, No. 8, 333–340, 1979.

[35] Wang, L., S. Zhang, C. Zhang, and Y. Zhou, "An improved deadbeat predictive current control based on parameter identification for PMSM," *IEEE Transactions on Transportation Electrification*, Vol. 10, No. 2, 2740–2753, 2024.

[36] Guo, X., S. Huang, P. Yu, J. Yang, and H. Wang, "Sliding mode control of IPMSM speed regulation system based on an improved double power reaching law and global fast terminal sliding mode observer," *Transactions of China Electrotechnical Society*, Vol. 38, No. 1, 190–203, 2023.